Multiscale Study of the Mechanism of Catalytic CO_2 hydrogenation: Role of the Ni(111) Facets

Pablo Lozano-Reis, Hèctor Prats, Pablo Gamallo, Francesc Illas and Ramón Sayós*

Departament de Ciència de Materials i Química Física & Institut de Química Teòrica i Computacional (IQTCUB), Universitat de Barcelona, C. Martí i Franquès 1, 08028 Barcelona, Spain

ABSTRACT

The molecular mechanism of CO_2 hydrogenation on Ni(111) surface has been thoroughly investigated by means of periodic density functional theory calculations including dispersion interactions along with accurate kinetic Monte Carlo simulations including lateral interactions between the adsorbates. The present reaction model involves 25 different species and a total of 86 elementary processes including adsorptions, desorptions, surface chemical steps and diffusions. The reaction network accounts for three different mechanisms for the reverse water gas shift reaction and three different mechanisms for methanation. The kinetic Monte Carlo simulations reveal that the reverse water gas shift reaction dominates the CO_2 hydrogenation on Ni(111) with no evidence of methane formation. The reaction proceeds mainly through the redox route with the carboxyl pathway also also active but to a lesser extent. Methane production is hindered by the $H + CO \rightarrow HCO$ endothermicity and the prohibitive energy barrier for CO dissociation implying CO desorption rather than evolution through the Sabatier reaction. A detailed comparison to earlier theoretical studies supporting the methanation reaction shows that some unreliable assumptions along with limited theoretical approaches biased the former conclusion.

KEYWORDS Reverse water gas shift reaction, Sabatier reaction, nickel (111), density functional theory, kinetic Monte Carlo, catalytic activity

INTRODUCTION

The continuous and drastic increase in the use of carbon-rich fossil fuels in response to the world energy demand has dangerously increased the amounts of atmospheric carbon dioxide with concomitant effects on the global warming of our climate system. Although a switch from fossil fuels toward different sources of green energies [1,2] would be desired, these cannot yet cover all the global energetic demand. In fact, it is expected that atmospheric CO_2 concentration will be still rising in the following years. Therefore, many efforts are being addressed towards the chemical conversion of CO_2 into new added-value chemicals of industrial interest, CO, CH_4, methanol and formaldehyde being the more investigated options [3-7]. The common step for all these processes is the CO_2 capture from flue gases through the so-called Carbon Capture and Storage (CCS) technologies [8-10]. Nowadays, this strategy seems to be suitable for industrial purposes that involves simultaneously reducing the environmental impact related to carbon dioxide emissions and generating chemicals that can be further used as energy carriers, thus, creating a cyclic energy economy where appropriate heterogeneously catalysed processes play an essential role.

In the last few decades, catalytic CO_2 hydrogenation has gained attraction towards the use of this greenhouse gas as an economic C_1 carbon source. Moreover, the Power-to-Gas (PtG) technology [11,12] has increased interest as a promising option to absorb and exploit surplus renewable energy. The PtG concept is based on using the excesses of renewable energies (i.e., excesses of solar power or wind power) for water splitting and then use the produced H_2 for CO_2 hydrogenation towards different chemicals. By choosing the metal and type of support used for the heterogeneous catalyst for CO_2 hydrogenation, it is possible to tune the selectivity towards a specific product. Among the possible chemicals that can be obtained from the CO_2 hydrogenation, methanol[13-23], methane[24-36] and CO[28,37-41] have woken increasing interest due to the various possible applications either as fuels or in syngas processes. Methanol is produced via CO_2 partial reduction using Au[13-15], Pd[16,17] or Cu-based catalysts,[18-20,22,23] methane is produced mostly using Ru,[25-27] Ni,[29-35] Pt,[24] or Pd-based catalysts[28] via the well-known Sabatier reaction and CO can be obtained through the reverse water gas shift reaction (RWGS) using Pt[37], Rh[38] Fe[39] or Ni-based catalysts.[40,41]

In the case of CO_2 hydrogenation, Ni is one of the most commonly used catalysts because of its relatively high activity and its economic viability compared to the noble metals.[42,43] It must be pointed out that while most of the experimental works deal with CO_2 hydrogenation on Ni-based, usually supported catalysts [29,35,40,41], theoretical studies focused on the idealized Ni(111) surface. [44-52] The reason being that it constitutes the most stable extended Ni surface and, thus, Ni(111) facets would predominate in the large Ni nanoparticles that are present in the industrial catalysts. However, in spite of the many studies published on the mechanism of the CO_2 hydrogenation on Ni(111), the overall picture is not yet fully understood with conflicting predictions regarding selectivity with respect to RWGS or Sabatier reactions.

From the experimental point of view there is only one study directly focusing on CO_2 hydrogenation on the Ni(111) surface. In this study, Heine et al.[35] used ambient-pressure X-ray photoelectron spectroscopy and identified OH and CO surface species, a clear indication that the RWGS reaction was occurring. Moreover,

these authors also reported the presence of atomic C, hence indirectly suggesting that the Sabatier reaction would also take place on this surface through the reduction of CO to C and its later hydrogenation to CH_4. However, they did not provide direct evidence regarding methane formation and no information is given regarding either turnover frequency (TOF) or the CO/CH_4 selectivity.

The number of theoretical studies dealing with CO_2 hydrogenation on Ni(111) is rather vast with different models being used as well. For instance, a cluster model study proposed that the $2CO \rightarrow C + CO_2(g)$ disproportionation step constitutes the key process for atomic carbon formation that can be further hydrogenated to methane.[46] On the other hand, Ren et al. [47] suggested three different mechanisms for CO_2 methanation, concluding that the CO dissociation mechanism was the most likely to occur. It is interesting to mention that available studies regarding CO methanation on Ni(111), can provide additional information for CO_2 hydrogenation, as many elementary steps are coincident for both reactions. Thus, Zhou et al.[45] studied the competition between the water gas shift (WGS) and the CO methanation reactions on Ni(111), concluding that WGS reaction was more likely than the methanation one. Similarly, Zhi et al. [44] investigated the CO methanation and proposed that the mechanisms through the HCO and HCOH species are the most favourable routes for methane formation. In a recent DFT study of RWGS reaction on Ni(111) and Ni(311) surfaces, Zhang et al.[49] suggested that Ni(311) should be more active than Ni(111) for surface redox mechanism in RWGS reaction. There are also combined experimental and theoretical studies although seldom using the same models system. For instance, Vrijburg et al.[53] studied CO_2 hydrogenation on bimetallic catalysts, Ni/TiO_2 and $NiMn/TiO_2$ were used in the experiments and $Mn_4O_4/Ni(111)$ and Ni(311) in the calculations. Both, experiments and calculations suggest a higher activity for the bimetallic catalysts. Very recently, Vogt et al.[48] reported an experimental and theoretical study for CO_2 hydrogenation catalysed by Ni. The experiments were performed over Ni catalyst supported on different metal oxides whereas the calculations were carried out for several Miller low index Ni ideal surfaces and included a rather limited microkinetic modelling. These authors provided experimental evidence that methane is formed over the supported Ni catalysts, a conclusion maintained by the theoretical study on the ideal surfaces.

In the present study we combine periodic DFT calculations including dispersion interactions with high-fidelity kinetic Monte Carlo (kMC) simulations to obtain an in-depth insight into the CO_2 hydrogenation mechanism on Ni(111) and to provide direct, unbiased, predictions of activity and selectivity towards both the RWGS and Sabatier reactions under relevant operating conditions. Macroscopic modelling through kMC or microkinetic simulations are being increasingly used in theoretical studies of heterogeneously catalysed reactions because they incorporate pressure and temperature effects beyond a purely thermodynamic picture. Indeed, temperature and pressure effects can have a decisive role in the catalytic performance. Even if both kMC and microkinetic simulations provide similar information regarding the macroscopic regime, we have chosen the former because they do not rely on the mean-field approximation and are spatially resolved, thus including adsorbate mobility and reaction dynamics in an explicit way.

COMPUTATIONAL METHODS AND MODELS

DFT calculations. The DFT-based calculations have been carried out using the Vienna Ab Initio Simulation Package (VASP) code[54-56] with the frozen-core augmented wave (PAW) method[57] to describe the interaction between the atomic cores and the valence electron density. Since the exact universal functional remains unknown, the choice of the density functional is always an open issue and a matter of discussion. In the view of recent benchmark studies,[61-60] showing that the rather recently proposed BEEF-vdW functional[61] provides an agreement with the available experimental data better than other commonly used functionals, we decided to use this functional that includes non-local correlation effect as well. For the scrutinized systems this functional exhibits mean absolute deviations usually lower than 0.3 eV, although depending on the training data considered.

Spin-polarization has been considered to account for the magnetic properties of nickel. The optimized nickel lattice parameter is 3.54 Å, in good agreement with the experimental value of 3.52 Å[62]. The Ni(111) surface— featuring hcp, fcc, bridge and top adsorption sites— has been modelled by a slab (3×3) supercell model containing 4 atomic layers with a 20 Å vacuum width between periodically repeated slabs, to avoid spurious interactions. The two bottom layers of the slab have been kept fixed at their bulk positions to provide an appropriate bulk environment to the two outermost surface atomic layers that have been allowed to fully relax in the geometry optimization calculations involving either the clean or adsorbate covered surface. A cut-off energy for the plane wave expansion of 415 eV and a (7×7×1) Monkhorst-Pack[63] ***k***-points mesh for sampling the first Brillouin zone have been used in all the calculations. A 10^{-5} eV threshold has been selected for the electronic energy optimization while ionic relaxation has been allowed until the forces acting on the atoms were smaller than 0.01 eV·Å^{-1}.

Transition states (TS) have been located by means of the Climbing-Image Nudged Elastic Band method[64,65]. The initial guesses for the employed intermediate images have been generated by means of the Atomic Simulation Environment package[66] using the Image Dependent Pair Potential procedure[67]. The located TS structures have been properly characterized by pertinent frequency analysis ensuring that they only exhibit one imaginary frequency. Frequency calculations have also been performed for all the adsorbed species to ensure that they correspond to minima in the potential energy surface. When calculating reaction rates (*vide infra*), low frequency modes below a cut-off value of 6.9 meV have been set to this cut-off value in order to approximate the entropy from a pseudotranslational/pseudorotational degree of freedom (see Section 1 in the Supporting Information for further details). The energy of an *i* gas-phase molecule ($E_{i(g)}$), has been calculated by placing one single molecule in an asymmetric box of (9×10×11) Å^3 considering only the Γ-point. We have used an asymmetric box to ensure convergence to the lowest energy state of the species. Then, the adsorption energy of any *i* of the considered 21 surface species ($E_{ads,i}$) has been calculated as follow:

$$E_{ads,i} = E_{i-slab} - E_{slab} - E_{i\,(g)} \qquad (1)$$

where E_{i-slab} is the energy of the i species adsorbed on the surface and E_{slab} is the energy of the relaxed pristine surface. With this definition, a negative value of $E_{ads,i}$ represents a favourable adsorption on the

surface. The energy barriers and reaction energies are computed, as usual, taking the difference between the total energy of TS and reactant optimized structures and between the total energy of adsorbed products and reactants in their optimized structure. Both reaction energies ($\Delta E_{0,r}$) and energy barriers ($\Delta E_0^{\neq}$) reported in this work include also the contribution from the zero-point vibrational energies calculated within the harmonic oscillator approximation. This contribution is also taken into account when considering adsorption/desorption rates of reactants and products and involves both gas phase and adsorbed species.

kMC simulations. The present reaction model involves 25 different species (i.e., 6 gas-phase molecules and 19 adsorbed intermediates) and a total of 86 processes, as shown in Figure 1. The kMC method[68,69] simulates the system time evolution at the molecular level, in such a way that each elementary process has an associated transition rate (i.e., adsorption rate, diffusion rate, reaction rate, *etc.*). In this work, we have used the graph-theoretical kMC approach[70] combined to cluster expansion Hamiltonians [71,72] for the adlayer energetics as implemented in the Zacros code (version 1.01).[70,71] A lattice model consisting on a two-dimensional hexagonal periodic grid of L×L points has been used to mimic the hexagonal symmetry of the Ni(111) surface. Each point in the lattice model corresponds to a coarse-grained site that represents a catalytic site of the Ni(111) surface (i.e., fcc, hcp, bridge or top sites). The convergence with respect to the lattice size has been verified by computing the steady-state TOFs and coverages with different L = 8, 12, 16 values, concluding that the results from a (8×8) lattice virtually coincide with those obtained using larger surface models. Consequently, the (8×8) lattice has been used in the subsequent calculations; further details are given in Section 2 in the Supporting Information. In this (8×8) lattice model, each adsorbed species can interact with their six nearest neighbours in the hexagonal periodic grid. Species that occupy a single adsorption site on the DFT calculations are considered to occupy a single site in the kMC lattice, while species that occupy two neighbouring adsorption sites in the DFT calculations are represented as bidentate adsorbates during the kMC simulations. For readers unfamiliar with the kMC method, we suggest the very recent tutorial from Andersen et al.[68]

In this study we have considered as reaction model an ideal mixture of two gas-phase reactants (i.e., CO_2 and H_2 at given partial pressures and temperature) continuously impinging on an initially empty and thermalized Ni(111) surface, where a long list of surface processes can take place, and afterwards, the formed products leave the surface region. Hence, the present model simulates a differential flow reactor with constant reactant flux and temperature. Therefore, reactants are allowed to adsorb and desorb, while products are only allowed to desorb. The reaction model involves the most relevant reaction mechanisms proposed in the literature, including three different reaction routes for the RWGS reaction and three different reaction routes for the Sabatier reaction. For completeness, we have also considered the possible formation of side products such as formaldehyde (CH_2O) and methanol (CH_3OH), although their formation is generally not observed on Ni-based catalysts. The total number of 86 processes included in our reaction model correspond to 36

reversible steps (i.e., adsorption, desorption or surface chemical reaction), which include both forward and reverse processes plus 5 irreversible desorption steps and 9 reversible but symmetric diffusion steps.

The expressions used to calculate the transition rates of all processes are described in detail in Section 3 of the Supporting Information. Mostly, Transition State Theory and DFT data were used. Due to the large number of species involved in our reaction model, we have truncated the cluster expansion to first nearest-neighbour two-body terms. The cluster expansion includes pairwise lateral interactions for all the reactants and products pairs as well as pairwise lateral interactions between the most relevant species during the simulations defined as species with significant coverage and key intermediate species. Overall, 19 different one-body terms and 50 different two-body terms are included in the cluster expansion, which are listed in Tables S3 and S4 of the Supporting Information, respectively. The one-body terms were calculated as the formation energies of the adsorbed species, and the two-body terms were obtained as the difference between the formation energies of the coadsorbed species and the formation energies of the isolated species. Further details regarding the calculation of formation energies or the cluster expansion used are given in Sections 4 and 5 of the Supporting Information, respectively. Note that our reaction model involves processes with very dissimilar energy barriers, resulting in reaction rates differing by several orders of magnitude. The concomitant difference in time scales has been handled by manually scaling the reaction rates of fast processes by using a scaling factor (i.e., $\alpha < 1$), and ensuring that such scaling does not affect the final results; this is further described in Section 6 of the Supporting Information. This pragmatic solution has been successfully applied in several previous kMC studies.[73-76]

For each operating condition, we have carried out 5 kMC simulation runs over an initially pristine Ni(111) surface using different random seeds. In this way, a larger part of the configuration space is explored, compared to running one single very long simulation. To obtain the final results, the resulting steady-state macroscopic properties such as TOFs and coverages have been averaged whereas the error bars have been taken as the standard deviation among the different kMC replicas. The total number of kMC steps was in the order of 10^8 for all working conditions. All the simulations have been performed using an initial CO_2 and H_2 reactant mixture with a 1:4 ratio at total pressures of 1 and 10 bar and temperatures of 573.15 K and 673.15 K, which are typical operating conditions.[4,48] Each simulation has been allowed to achieve a steady-state in which no-variations of the surface coverage for intermediate species are observed, with the exception of small fluctuations resulting from the stochastic nature of the method. Then, the TOF is calculated as the number of product species formed per site and unit time. Moreover, to unveil the dominant reaction mechanism that controls the reaction, the event frequency of the different processes has been analysed.

RESULTS AND DISCUSSION

DFT results. We start by noting that a total of 21 adsorbed species and 7 gas-phase species are involved in the considered mechanisms for the RWGS and Sabatier reactions. The adsorption energy for all the species has been calculated for each of the four possible high symmetry adsorption sites (see Section 7 of the

Supporting Information for further details). Table 1 summarizes the adsorption energies for all the species in their optimized structures at the most favourable site along with already published data for comparison.[44,45,51,52] The present results are in close agreement with published data, even though some discrepancies are found, not only on the adsorption energy values but also on the reported most stable adsorption sites for some adsorbates, especially for the largest ones. In general, PBE[45,52] and PW91[44] functionals tend to overestimate adsorption energies with predicted values larger than those obtained from RPBE[51] or BEEF-vdW (Table 1). Moreover, there is a rather good agreement between the calculated CO heat of adsorption (i.e., -1.55 eV at 300 K for 0.11 ML) and the experimental value of ~ -1.3 eV on hollow sites at 0.25 ML coverage and $300 \leq T \leq 425$ K [77, 78.] Note that the higher the coverage the lower the adsorption energy due to the repulsive CO-CO interaction. In addition, the present study nicely reproduces the experimental heat of adsorption hollow > bridge > ontop trend (see table S7 of the Supporting Information).

For larger adsorbates such as CH_2OH, CH_3OH, HCOO and t-COOH, the PBE and PW91 adsorption energies are closer to the present BEEF-vdW calculated values. However, this could be a result of error compensation in all previously reported DFT studies on this system, since PBE/PW91 overbinding is still present but the dispersion contributions are neglected. These interactions are especially important for the largest intermediates and physisorbed (non-polar) molecules such as CO_2 or CH_4, and its inclusion can produce very large changes in the predicted reaction rates, as it has been shown for the WGS reaction on Cu(321).[79]

To provide unambiguous insight regarding the mechanism that governs CO_2 hydrogenation on the Ni(111) surface, all possible relevant reaction mechanisms reported in the literature have been explicitly considered with the complete reaction network summarized in Figure 1. Table 2 reports the calculated reaction energies ($\Delta E_{0,r}$) and energy barriers ($\Delta E_0^{\neq}$) for all considered elementary steps, along with already published data to facilitate their comparison. Note that the present values include dispersion interactions and the zero-point energy (ZPE) term while both are neglected in previous works. With this information at hand, three different mechanisms for the RWGS reaction and three different mechanisms for the Sabatier reaction can be distinguished, which are discussed on the basis of the corresponding calculated potential energy diagrams (PEDs). The possible desorption of some side species such as formaldehyde and methanol are also accounted for although not included in the reported PEDs.

The three proposed mechanisms for the RWGS reaction are the reverse of the redox, formate and carboxyl pathways in the WGS reaction, respectively (see Figure 2 for PEDs), which differ in the way CO is produced. In the redox pathway (Figure 2a), CO is directly produced by CO_2 dissociation (i.e., R4, $\Delta E_0^{\neq}$ = 0.86 eV) and water is formed by hydrogenation of adsorbed atomic O. The formate pathway (Figure 2b) involves the formation of HCOO by reaction between CO_2 and H (R5, $\Delta E_0^{\neq}$ = 1.06 eV). Next, HCOO dissociates to produce adsorbed HCO and O species (R13, $\Delta E_0^{\neq}$ = 1.39 eV), with subsequent dissociation of the former species (R15, $\Delta E_0^{\neq}$ = 0.21 eV) leading to the formation of adsorbed CO. Again, water is formed by hydrogenation of adsorbed O. Finally, the carboxyl pathway (Fig. 2c) is related to the formation of COOH. In this mechanism, adsorbed CO_2 and H react to produce COOH (R6, $\Delta E_0^{\neq}$ = 1.35 eV) and then, CO can be

produced either by direct COOH dissociation (R11, $\Delta E_0^{\neq}$ = 0.50 eV), or via the COH intermediate (R12, $\Delta E_0^{\neq}$ = 1.28 eV and R17, $\Delta E_0^{\neq}$ = 1.21 eV, respectively).

Among the mechanisms proposed in the literature for the RWGS reaction, the redox pathway is by far the most favoured route for CO production, since the energy barrier for CO_2 dissociation is lower than those for HCOO or COOH formation, and it is an unimolecular step, which makes it more probable to occur than a bimolecular step, in agreement with previously reported results.[49,50,52] Both, formate and carboxyl pathways, involve hydrogen assisted steps and they will be only feasible at high H coverage. Among them, HCOO formation (R5) has lower energy barrier than COOH formation (R6). However, after HCOO formation, the system can go backwards because the reverse energy barrier for this process is lower than that for further dissociation to produce HCO (R13). Conversely, if COOH is formed, it will dissociate mainly to produce CO (R11) compared with reverse R6 and R12 processes. Therefore, it is not clear which of these two mechanisms will dominate, although the current DFT calculations clearly suggest that both of them will be hardly relevant and that the redox mechanism should prevail, suggesting CO_2 dissociation as the rate-determining step.

The three proposed mechanisms for the Sabatier reaction are the carbon hydrogenation pathway, the HCO hydrogenation pathway, and the COH hydrogenation pathway, as also summarized in Figure 2. These mechanisms differ in the way CH_3 is produced, which is finally hydrogenated to methane. In all mechanisms it is assumed that CO is formed via the redox pathway and then, it reacts to produce the key intermediate of each mechanism. Note that key intermediates could also be obtained from other elementary steps (see Figure 1) that are not included in the PEDs. The C hydrogenation pathway (Figure 2d) starts with the formation of atomic C species, either from CO dissociation (R14, $\Delta E_0^{\neq}$ = 2.98 eV) or from COH dissociation (R18, $\Delta E_0^{\neq}$ = 1.81 eV), and further hydrogenation to produce CH_3. The HCO hydrogenation pathway (Figure 2e) is related to the formation of the key intermediate HCO via the HCOO dissociation (R13, $\Delta E_0^{\neq}$ = 1.39 eV) or from H+CO hydrogenation (reverse R15, $\Delta E_0^{\neq}$ = 1.47 eV). Next, HCO is hydrogenated to CH_3O, which can dissociate to produce CH_3. Finally, the COH hydrogenation pathway (Figure 2f) involves the formation of the key intermediate COH via the COOH dissociation (R12, $\Delta E_0^{\neq}$ = 1.28 eV) or the CO+H hydrogenation (reverse R17, $\Delta E_0^{\neq}$ = 2.33 eV). Next, COH is further hydrogenated to methanol which then, dissociates to produce CH_3. Apart from these three main mechanisms, there are many elementary interconnecting steps, which are responsible for the high complexity of the CO_2 hydrogenation landscape on Ni(111), as shown in the reaction network in Figure 1. For instance, dehydroxylation of CH_xOH species leads to CH_x species, providing hybrid reaction routes combining the COH hydrogenation and C hydrogenation mechanisms. Similarly, CH_xO species can deoxygenate to produce CH_x species, providing connections between the HCO and C hydrogenation mechanisms. Note also that, in addition to the final products of the RWGS reaction (i.e., $CO_{(g)}$ and $H_2O_{(g)}$) and the Sabatier reaction (i.e., $CH_{4(g)}$ and $H_2O_{(g)}$), other intermediate species are present which can desorb, leading to side products. This is the case for methanol ($CH_3OH_{(g)}$) and formaldehyde ($CH_2O_{(g)}$).

By inspecting all the different possibilities provided by the full reaction network, the most feasible reaction route to $CH_{4(g)}$ production seems to be through CO formation via the redox mechanism, followed by

its possible hydrogenation to HCO (reverse R15, $\Delta E_0^{\neq}$ = 1.47 eV). Then, in a H dominated regime, HCO could be further hydrogenated to CH_2O (R22, $\Delta E_0^{\neq}$ = 0.82 eV), then deoxygenated to CH_2 (R30, $\Delta E_0^{\neq}$ = 0.96 eV), and finally, hydrogenated to $CH_{4(g)}$. On the other hand, in a system with low H coverage and high availability of surface free sites, HCO could be deoxygenated to CH (R16, $\Delta E_0^{\neq}$ = 1.10 eV) and finally, hydrogenated to $CH_{4(g)}$. Hence, the most favourable route for methane production would involve the RWGS redox mechanism to form CO, followed by a combination of the HCO and C hydrogenation mechanisms. However, there are some thermodynamic and kinetic aspects that make $CH_{4(g)}$ production hardly achievable. The first challenge is the presence of bimolecular hydrogenation steps, which are obviously much slower than several unimolecular steps. Moreover, if CO is hydrogenated to HCO through reverse R15, the system will probably move backwards, since the energy barrier in the backward direction for this elementary step is of 0.21 eV only. Moreover, it is very likely that CO will desorb rather than follow the reaction path towards methane, methanol or formaldehyde. The main reason is that, once a CO molecule is formed, it will desorb (R2, $\Delta E_{0,r}$ = $\Delta E_0^{\neq}$= 1.58 eV) rather than react to form C, COH or HCO. The first two processes are kinetically impeded due to extremely high energy barriers ($\Delta E_0^{\neq}$ = 2.98 and 2.33 eV, respectively). On the other hand, although the HCO formation process through reverse R15 has an energy barrier ($\Delta E_0^{\neq}$ = 1.47 eV) similar to CO desorption, it is a bimolecular process, hence requiring a neighbouring H adsorbate. Even in the case of a H dominated regime, where the concentration of HCO could be significant, the system would move again backwards, due to its very low energy barrier ($\Delta E_0^{\neq}$ = 0.21 eV).

Overall, a first inspection of the full DFT energy landscape seems to suggest that the RWGS reaction should dominate on Ni(111) with $CO_{(g)}$ being the main product through the redox mechanism. However, as mentioned in Section 1, a more quantitative and rigorous description of the kinetics of such a complex reaction network requires to simultaneously consider all involved steps at working conditions of pressures and temperatures; this is precisely the aim of the next section.

kMC results. To gain further insight into the mechanism of CO_2 hydrogenation on Ni(111), kMC simulations have been carried out at typical operating conditions for Sabatier reaction on Ni-based catalysts;[4] thus pressures of 1 and 10 bar, and temperatures of 573.15 and 673.15 K are considered. These simulations involved a CO_2/H_2 mixture with a 1:4 ratio although additional runs with a 1:1 CO_2/H_2 mixture lead to the same results. We start by analysing the TOF and the event frequencies of the main elementary steps, which will allow us to provide estimations of catalyst activity and selectivity, and also to unveil the dominant mechanism that controls the reaction.

The TOFs and event frequencies of the main elementary steps at the four different operating conditions are shown in Figure 3. Clearly, no methane formation is observed at any of the studied conditions, as inferred also from the DFT calculations. Even if the simulations show that some HCO is produced through CO hydrogenation, which could be an important intermediate towards methane production, the energy barrier for HCO dissociation is very small thus evolving back to CO, hence hindering the CH formation and subsequently,

the hydrogenation to methane. Figure 3 clearly shows that CO_2 hydrogenation on Ni(111) is dominated by the RWGS through the redox route (R4 step in Figure 1), also in agreement with what is inferred from the analysis of the DFT energy profiles. Interestingly, the carboxyl pathway is also active with COOH being produced by reaction of CO_2 either with H (R6) or OH (R7). Nevertheless, COOH dissociates to produce CO through R11 step. In any case, the frequency of CO formation through the carboxyl pathway is between 2-3 orders of magnitude smaller than through the redox pathway. This clearly suggests that the CO_2 dissociation step is the rate-determining step. This has been confirmed by calculating the Campbell's degree of rate control[80] for the three competing processes starting from CO_2 (i.e., R4, R5 and R6) at several temperatures (see table S8 in the Supporting Information for further details).

Regarding the formate pathway, Figure 3 shows that indeed HCOO is formed but evolving backwards to CO_2, meaning that this third mechanism does not contribute at all towards the RWGS reaction. Figure 3 also shows that, despite the scaling down of the adsorption/desorption step rates, the system spends most of the simulation time precisely adsorbing and desorbing CO_2. This result agrees with the low desorption energy of CO_2 (0.14 eV including ZPE correction) significantly lower that the energy barriers for other CO_2-related processes such as R4-R10, also much less accessible because they are mainly bimolecular. At 573 K, the second most time-consuming process is H_2 dissociative adsorption and its subsequent H recombination back to $H_{2(g)}$. Although the energy barrier for this recombination is quite high (i.e., reverse R3, $\Delta E_0^{\neq} = 0.86$ eV), it is lower than other energy barriers for H involving steps (e.g., with O, OH, CO_2 or CO, the species with the highest coverages; *vide infra*). Moreover, it is more likely that neighbouring H-H pairs are found in the lattice due to the dissociative $H_{2(g)}$ adsorption, in comparison to other pairs such as H-O, H-CO_2 or H-CO. These event frequency diagrams also show that when a diffusing H atom finds an O atom arising from CO_2 dissociation, the system spends a considerable amount of time forming OH (R35) and going backwards. Compared to the others, the relative event frequency for this step increases with temperature because it is an endothermic process.

Water is mainly formed through OH hydrogenation (i.e., R36, $\Delta E_0^{\neq} = 1.25$ eV), although to a lower extent it is also formed by the disproportionation of two neighbouring OH species (i.e., R37, $\Delta E_0^{\neq} = 0.42$ eV). The energy barrier for the later process is much lower, but its event frequency is 2-3 orders of magnitude lower because of the very low OH coverage (*vide infra*). Finally, the kMC simulations evidence that changes either on the reaction temperature or on the partial pressure of reactants have no significant effect, other than affecting the event frequency of all processes in a fairly homogeneous way. Obviously, as the temperature or pressure are increased, the overall TOF also increases (see Figure 3).

The steady-state (final) coverage of the main surface species are reported in Table 3. At all studied reaction conditions, the coverage of all the intermediate species is below 1%, with the solely exception of atomic H, which is around 7-17% depending on the T and P values. These results are a consequence of the too weak adsorption of reactants, intermediates and products over Ni(111). According to *Le Sabatier* principle, catalysts that present too weak or too strong binding for adsorbed species exhibit low activity. This is precisely

what is observed, the TOF values reported in Figure 3 at different reaction conditions are all very low. These low values could be seemingly in contrast with the experimental evidence that Ni-based catalysts are active towards the RWGS and Sabatier reactions.[29-32,40,41] Therefore, one can conclude that the active sites are not located on the Ni(111) facets and that the role of the Ni support, the size and morphology of Ni nanoparticles are likely to play an important role on the overall process.

We have also computed the partial orders of reaction with respect to both reactants and the apparent activation energy of the overall reaction by performing different simulations at varying temperatures and pressures. The calculated partial orders at 673.15 K for CO_2 and H_2 are 0.82 and 0.21, respectively (see Section S9 of the Supporting Information for further details). The calculated apparent activation energy at 1 bar and 10 bar are 0.82 and 0.85 eV, respectively (see Section S10 in the Supporting Information). Note that these values are very similar to the energy barrier of the CO_2 dissociation step (i.e., 0.86 eV), thus, confirming that this is indeed the rate-determining step. Unfortunately, to our knowledge, the experimental apparent activation energy and partial orders of reaction have not been reported.

Several theoretical studies[44,47,48] and one experimental work[35] have claimed that CO_2 hydrogenation on Ni(111) should produce methane. It is important to point out that the experimental study supports this claim solely by the presence of a peak at 283.3 eV attributed to adsorbed C, which is then taken as indication that methanation could follow. However, the same study provides compelling evidence that CO_2 leads to CO through the RWGS, which is in agreement with the present results. The analysis of the present kMC simulations shows that, under the scrutinized conditions, methanation will not take place on Ni(111). The main bottleneck for methanation is that CO desorption is much more favourable than any other competing process evolving to methane such as HCO formation (reverse R15, $\Delta E_0^{\neq}$ = 1.47 eV) or CO dissociation (R14, $\Delta E_0^{\neq}$ = 2.98 eV); see also Figure 2d and 2e. That CO desorption blocks methane formation is also supported by accurate measurements of the heat of adsorption of CO on Ni(111) of ~ -1.3 eV [77,78] , even lower than the value predicted by the present or previous DFT calculations (see Table 1). Nevertheless, since too strong CO adsorption energies could be obtained as a consequence of the selected functional, we have done a sensitivity analysis of the CO desorption process. We concluded that even when the CO desorption rate is slowed by 2 orders of magnitude (corresponding to a 0.26 eV stronger CO adsorption energy), no methane is formed, and only CO is produced (see Section S11 of the Supporting Information for further details).

Additional support to the present findings comes from the work of Catapan et al.[52] on the WGS reaction over both flat Ni(111) and stepped Ni(211) surfaces which shares the reverse R15 and R14 elementary steps. These authors report energy barriers and reaction energies similar to those reported in the present study, thus supporting that methanation on Ni(111) and Ni(211) surfaces is unlikely to occur. For the Ni(111) case, they proposed the redox pathway involving the route through direct CO_2 dissociation as the most plausible mechanism for the RWGS reaction, in agreement with the present findings. Note that Zhang et al.[49] also reported the redox pathway as the most plausible mechanism for the RWGS reaction on the Ni(111) and Ni(311) surfaces, but from their data it is not possible to predict whether Ni(311) will be active for

methanation. However, the study of Vrijburg et al.[53] that couples DFT calculations with microkinetic modelling shows that the Ni(311) surface is active for methane formation. They found that for the Ni(311) surface the COH intermediate is a possible source of atomic C, which is further hydrogenated to methane, although this would not be possible for Ni(111) or Ni(211) surfaces, indicating that not all stepped surfaces may exhibit methanation activity.

Regarding earlier theoretical studies on CO_2 hydrogenation, Choe et al.[44] claimed that CO disproportionation is a possible source of methane formation. However, their result is an artefact arising from excessively large adsorption energies for CO and CO_2. In our reaction network, this CO unusual disproportionation step has not been included, precisely because the energy barrier for CO disproportionation is higher[44,45,46] than required for CO desorption. Ren et al.[47] proposed an optimal mechanism for methane production from CO_2 via a route involving CO_2 and CO consecutive dissociations. However, they did not consider the much more favourable CO desorption process and other important and competing processes for CO reactions, that should notably affect the final reaction products. In a recent experimental and theoretical study, Vogt et al.[48] presented a microkinetic modelling for CO_2 conversion over several Ni facets, concluding that some methanation could occur over these unsupported Ni facets. However, their reaction network was quite incomplete and involved several important limitations. For instance, their DFT study relied on the PBE functional, a robust and broadly used one, but neglected dispersion energies and lateral interactions. Moreover, even more critical was neglecting the CO desorption step into the microkinetic modelling. As a result, an artificially too large CO coverage was obtained which favoured the H-assisted CO dissociation process and hence the CH_4 formation.

Additional studies involving CO methanation and the WGS reaction on Ni(111) could give valuable additional information for understanding much better the CO_2 hydrogenation reaction. Zhou et al.[45] suggested that the HCO route was the most favourable pathway for methane production, although this intermediate was more likely to undergo the WGS reaction rather than the methanation reaction. However, these authors neglected the HCO hydrogenation step to CH_2O, which at high H coverages would be more feasible than the HCO dissociation to CH + O. Additionally, and more significantly, they also neglected the possible HCO dissociation to CO + H, which clearly hinders the Sabatier reaction as shown in the present work. Similarly, Zhi et al.[44] proposed HCO and HCOH dissociation steps as the most favourable routes for methane formation from CO hydrogenation, but they did not consider the possible CH_2O formation nor the low-energy barrier of HCO dissociation to form CO + H, which plays an important role. Moreover, since their energy barrier for CO hydrogenation to HCO was lower than for CO desorption, they also neglected the CO desorption process. The present results clearly confirm that CO desorption is a key step than cannot be neglected as it drives the CO_2 hydrogenation on Ni(111) to the RWGS reaction rather than to the Sabatier reaction. The importance of both CO desorption and HCO formation in tuning the selectivity from CO to CH_4 as it has been also shown in CO_2 hydrogenation over Pt, Pt/SiO_2 and Pt/TiO_2.[37]

CONCLUSIONS

DFT calculations along with kMC simulations have been performed to unravel the molecular mechanism of CO_2 hydrogenation on Ni(111), to determine the main products and to provide unbiased meaningful insights regarding the elementary steps governing the reaction. The reaction energies and energy barriers for a total of 86 elementary processes, conforming a complete reaction network, have been obtained. These correspond to three possible mechanisms for the RWGS reaction and three possible mechanisms for the Sabatier reaction. Among all the proposed mechanisms for the RWGS reaction, the redox pathway is by far the most favoured route to $CO_{(g)}$ production. This is because the energy barrier for CO_2 dissociation is lower than those for HCOO or COOH formation, and that it corresponds to a unimolecular process. For the case of the HCOO and COOH routes, the analysis of the PEDs alone is not sufficient to provide a conclusive idea regarding which pathway is preferred. We have also analysed the most feasible route for methane production, which involves the RWGS redox mechanism to form CO species, followed by a combination of the HCO and C hydrogenation mechanisms. However, the results show that several thermodynamic and kinetic aspects make $CH_{4(g)}$ production hardly achievable. In particular, we mention the presence of bimolecular hydrogenation steps, the very low energy barrier for the HCO → CO + H process, and the very likely CO desorption.

The present accurate kMC simulations have confirmed that no methane is formed on Ni(111) at any of the operating conditions studied, in contrast to what has been suggested in some earlier DFT and microkinetic studies based on some unreliable assumptions. kMC simulations also show that the RWGS reaction dominates mainly through the redox mechanism, but also through the carboxyl mechanism to a lesser extent. We have also confirmed that the CO_2 dissociation step is clearly the only rate-determining step. Therefore, we conclude that methane production observed experimentally on Ni-based catalysts is not due to the large presence of Ni(111) facets of the Ni nanoparticles and it should be likely a result of other contributions involving a possible synergic effect between the Ni particle and the support and also the existence of other sites that may be present depending on the particle morphology. This call for subsequent studies on the effect of the support and low coordinated sites on the CO_2 hydrogenation reaction.

ASSOCIATED CONTENT

Supporting Information

The supporting Information is available free of charge on the ACS Publications website at DOI: XXXX.

Information about the frequency scaling (Sec. S1), the lattice model used (Sec. S2), the reaction rates (Sec. S3) and the formation energies calculations (Sec. S4), the cluster expansion Hamiltonians used (Sec. S5), how fast processes have been scaled (Sec. S6), the adsorption energies of the species at different adsorptions sites (Sec. S7), how the Campbell's degree of rate control is calculated (Sec. S8), the reactants' partial orders of reaction (Sec. S9), the apparent activation energies (Sec. S10), the CO sensitivity analysis (Sec. S11), details about the kMC simulations (Sec. S12) and the structure of all

minima and transition states (Sec. S13). Optimized structures (i.e., VASP CONTCAR files) of all relevant stationary points and Zacros input files for the kMC simulations have been also made available on a public GitHub repository: https://github.com/plozanore/DFT_-_kMC_CO2_-_H2_Ni_111

AUTHOR INFORMATION

Corresponding Author

*E-mail for R.S.: r.sayos@ub.edu.

ORCID

Pablo Lozano-Reis: 0000-0001-9809-8023

Hèctor Prats: 0000-0003-4991-253X

Pablo Gamallo: 0000-0002-8531-8063

Francesc Illas: 0000-0003-2104-6123

Ramón Sayós: 0000-0001-6627-7844

Notes

The authors declare no competing financial interest.

ACKNOWLEDGMENTS

This research is supported by the Spanish Ministry of Science, Innovation and Universities through grants RTI2018-094757-B-I00, RTI2018-095460-B-I00, MCIU/AEI/FEDER, UE and MDM-2017-0767, and in part, by the *Generalitat de Catalunya* (2017SGR13 and XRQTC). P. L-R. acknowledges *Generalitat de Catalunya* for a predoctoral 2019 FI-B 00061 grant. P. G. is indebted to the *Serra Hunter* programme for supporting his professorship and F. I. acknowledges additional support from the 2015 ICREA Academia Award for Excellence in University Research. Computational resources provided by *Consorci de Serveis Universitaris de Catalunya* (CSUC, former CESCA) are gratefully acknowledged.

Table 1. Adsorption Energies (without ZPE) of Intermediate Species in Their Most Favourable Site. The Adsorption Sites of Literature Are Assumed to Be the Same Unless It Is Specified. All Values Are in eV.

Species, i	site	$E_{ads,i}$				
		This work	RPBE [51]	PBE [45]	PBE [52]	PW91 [44]
C	hcp	-6.35	-6.00	-6.89	-6.61	
CH	fcc	-5.94	-5.90*	-6.41	-6.84	-6.47
CH_2	fcc	-3.64	-3.30	-4.03	-4.07	
CH_2O	fcc	-0.58	-0.20*			-0.84
CH_2OH	top-top	-1.47	-1.00*	-1.56*		-1.68*
CH_3	fcc	-1.64	-1.30	-1.89		-1.94
CH_3O	fcc	-2.59	-1.90			-2.75
CH_3OH	top-top	-0.36	-0.03*			-0.37*
CH_4	top	-0.13	0.13[b]			
CO	hcp	-1.61	-1.50	-1.93	-2.09	-1.91
CO_2	top	-0.16	0.03*	-0.01*	-0.12*	
COH	hcp	-4.02	-2.10	-4.39	-4.42*	-4.45
H	fcc	-2.75	-2.80	-2.80	-2.77	-2.78
H_2	fcc/hcp	-0.68[a]	-0.95[c]	-0.25*		
H_2O	top	-0.26	-0.02*	-0.27	-0.47	-0.33
HCO	fcc	-2.05	-1.80*	-2.27	-2.49*	-2.36*
HCOH	fcc	-2.65	-2.40	-3.88		-3.91*
HCOO	top-top	-2.93		-2.88	-3.02	
OH	fcc	-3.22	-2.50	-3.27	-3.34	-3.54
O	fcc	-5.30	-4.50	-5.39	-4.81	-5.76
t-COOH	top-top	-2.13	-2.30*	-2.25*	-2.54*	

[a]The calculated value corresponds to the dissociative adsorption of H_2 with an H on the fcc site and the other H on an hcp site. [b]The literature value corresponds to the CH_4 dissociative adsorption into CH_3 and H. [c]The literature value corresponds to the H_2 dissociative adsorption into two H. Both literature values are calculated at T = 800 K and P = 1 bar and considering species at infinite distance. *Adsorption energy corresponding to a different adsorption site than the one presented in this study.

Table 2. Reaction Energies ($\Delta E_{0,r}$) and Energy Barriers ($\Delta E_0^{\neq}$) for All The Considered Processes Including the Zero-Point Energy Term Along with Relevant Published Data. Backward Energy Barriers Are Also Shown between Parenthesis. Note That Literature Values (i.e., $\Delta E^{\neq}$) Do Not Include The ZPE term. The * Symbol Represents A Free Adsorption Site. All Values Are in eV.

	This work		Literature values		
	$\Delta E_{0,r}$	$\Delta E_0^{\neq}$	$\Delta E^{\neq}$		
ID: surface process			PBE [45]	PW91 [44]	PBE [52]
R1: $CO_{2(g)} + * \rightleftharpoons CO_2$	-0.14	0.0 (0.14)	0.0 (0.01)		0.12 (0.0)
R2: $CO \rightarrow CO_{(g)} + *$	1.58	1.58 (0.0)	1.90 (0.0)	1.91 (0.0)	2.09 (0.0)
R3: $H_{2(g)} + 2* \rightleftharpoons 2H$	-0.60	0.26 (0.86)	0.01 (0.82)	0.13 (1.18)	0.08 (1.37)
R4: $CO_2 + * \rightleftharpoons CO + O$	-0.69	0.86 (1.55)	0.60 (1.56)		0.57 (1.53)
R5: $CO_2 + H \rightleftharpoons HCOO$	0.04	1.06 (1.02)	0.86 (0.99)		0.71 (1.05)
R6: $CO_2 + H \rightleftharpoons COOH$	0.51	1.35 (0.84)	1.11 (0.93)		0.80 (0.88)
R7: $CO_2 + OH \rightleftharpoons COOH + O$	0.35	0.47 (0.12)	0.19 (0.20)		1.06 (1.30)
R8: $CO_2 + H_2O \rightleftharpoons COOH + OH$	0.17	0.20 (0.03)	0.0 (0.0)		0.0 (0.0)
R9: $CO_2 + OH \rightleftharpoons HCOO + O$	-0.12	1.70 (1.82)	1.42 (1.75)		1.22 (1.62)
R10: $CO_2 + H_2O \rightleftharpoons HCOO + OH$	-0.31	1.61 (1.92)	1.33 (1.88)		1.22 (1.81)
R11: $COOH + * \rightleftharpoons CO + OH$	-1.04	0.50 (1.54)	0.44 (1.40)		0.50 (1.22)
R12: $COOH + * \rightleftharpoons COH + O$	-0.08	1.28 (1.36)			1.50 (1.41)
R13: $HCOO \rightleftharpoons O + HCO$	0.53	1.39 (0.86)	1.14 (0.73)		1.26 (0.74)
R14: $CO + *\rightleftharpoons C + O$	1.43	2.98 (1.55)	2.88 (1.60)	3.74 (2.32)	3.01 (1.59)
R15: $HCO + * \rightleftharpoons CO + H$	-1.26	0.21 (1.47)	0.19 (1.44)	0.21 (1.38)	0.20 (1.35)
R16: $HCO + * \rightleftharpoons CH + O$	-0.31	1.10 (1.41)	1.04 (1.54)	1.16 (1.44)	1.28 (1.43)
R17: $COH + * \rightleftharpoons CO + H$	-1.12	1.21 (2.33)	0.95 (1.91)	1.02 (1.94)	0.85 (1.81)
R18: $COH + * \rightleftharpoons C + OH$	0.47	1.81 (1.34)	1.86 (1.34)	2.01 (1.35)	2.07 (1.46)
R19: $C + H \rightleftharpoons CH + *$	-0.49	0.78 (1.27)	0.86 (1.39)	0.92 (1.38)	0.91 (1.32)
R20: $CH + H \rightleftharpoons CH_2 + *$	0.31	0.65 (0.34)	0.74 (0.36)	0.74 (0.40)	
R21: $CH_2 + H \rightleftharpoons CH_3 + *$	-0.08	0.60 (0.68)	0.63 (0.66)	0.77 (0.85)	
R22: $HCO + H \rightleftharpoons CH_2O + *$	0.37	0.82 (0.45)		0.53 (0.29)	
R23: $HCO + H \rightleftharpoons HCOH + *$	0.60	1.13 (0.53)	1.14 (0.71)	0.92 (0.58)	
R24: $COH + H \rightleftharpoons HCOH + *$	0.73	0.88 (0.15)	0.83 (0.10)		
R25: $HCOH + * \rightleftharpoons CH + OH$	-0.75	0.72 (1.47)	0.72 (1.45)	0.79 (1.26)	
R26: $HCOH + H \rightleftharpoons CH_2OH$	0.22	0.63 (0.41)	0.87 (0.53)	0.87 (0.62)	
R27: $CH_2OH \rightleftharpoons CH_2 + OH$	-0.67	0.71 (1.38)	0.65 (1.35)	0.85 (1.23)	
R28: $CH_2OH + H \rightleftharpoons CH_3OH + *$	-0.29	0.74 (1.03)			

R29: $CH_2O + H \rightleftharpoons CH_2OH$	0.45	1.00 (0.55)		1.06 (0.76)	
R30: $CH_2O + * \rightleftharpoons CH_2 + O$	-0.38	0.96 (1.34)		1.41 (1.57)	
R31: $CH_2O + H \rightleftharpoons CH_3O + *$	-0.33	0.52 (0.85)		0.65 (1.01)	
R32: $CH_3O + * \rightleftharpoons CH_3 + O$	-0.14	1.36 (1.50)		1.53 (1.57)	
R33: $CH_3O + H \rightleftharpoons CH_3OH$	0.48	1.43 (0.95)		1.31 (0.85)	
R34: $CH_3OH \rightleftharpoons CH_3 + OH$	-0.46	1.80 (2.26)			
R35: $O + H \rightleftharpoons OH + *$	0.16	1.28 (1.12)	1.17 (0.97)	1.21 (1.15)	1.16 (1.01)
R36: $OH + H \rightleftharpoons H_2O + *$	0.35	1.25 (0.90)	1.27 (0.86)	1.32 (1.02)	1.15 (0.90)
R37: $OH + OH \rightleftharpoons O + H_2O$	0.19	0.42 (0.23)	0.48 (0.27)		0.0 (0.0)
R38: $H_2O \rightarrow * + H_2O_{(g)}$	0.20	0.20 (0.0)	0.27 (0.0)	0.33 (0.0)	0.47 (0.0)
R39: $CH_3 + H \rightarrow CH_{4(g)} + 2*$	-0.22	0.87 (1.09)	0.0 (0.03)	0.96 (1.13)	
R40: $CH_3OH \rightarrow CH_3OH_{(g)} + 2*$	0.31	0.31 (0.0)		0.37 (0.0)	
R41: $CH_2O \rightarrow CH_2O_{(g)} + *$	0.58	0.58 (0.0)		0.83 (0.0)	
D1: $C_{fcc} + * \rightleftharpoons C_{hcp} + *$	-0.04	0.31 (0.35)			
D2: $O_{fcc} + * \rightleftharpoons O_{hcp} + *$	0.10	0.42 (0.32)			
D3: $H_{fcc} + * \rightleftharpoons H_{hcp} + *$	0.02	0.12 (0.10)			
D4: $CO_{fcc} + * \rightleftharpoons CO_{hcp} + *$	-0.01	0.11 (0.12)			
D5: $OH_{fcc} + * \rightleftharpoons OH_{hcp} + *$	0.09	0.19 (0.10)			
D6: $H_2O_{top} + * \rightleftharpoons H_2O_{top} + *$	0.00	0.08 (0.08)			
D7: $CH_{fcc} + * \rightleftharpoons CH_{hcp} + *$	0.02	0.32 (0.31)			
D8: $CH_{2fcc} + * \rightleftharpoons CH_{2hcp} + *$	0.04	0.19 (0.15)			
D9: $CH_{3fcc} + * \rightleftharpoons CH_{3hcp} + *$	0.02	0.15 (0.13)			

Table 3. Coverage Value of Some Species During the Simulations at the Different Working Conditions.

Coverage (θ)	T= 573.15 K P_{H_2}= 0.8 bar P_{CO_2}= 0.2 bar	T= 573.15 K P_{H_2}= 8 bar P_{CO_2}= 2 bar	T= 673.15 K P_{H_2}= 0.8 bar P_{CO_2}= 0.2 bar	T= 673.15 K P_{H_2}= 8 bar P_{CO_2}= 2 bar
θ_H	12.69 ± 0.08	17.33 ± 0.06	7.69 ± 0.06	12.36 ± 0.09
θ_{CO}	0.031 ± 0.004	0.140 ± 0.019	0.007 ± 0.003	0.020 ± 0.004
θ_O	0.170 ± 0.011	0.227 ± 0.011	0.675 ± 0.028	0.810 ± 0.024
θ_{CO_2}	0.769 ± 0.008	0.926 ± 0.018	0.695 ± 0.011	0.775 ± 0.023
θ_{OH}	0.007 ± 0.004	0.023 ± 0.006	0.055 ± 0.004	0.076 ± 0.004

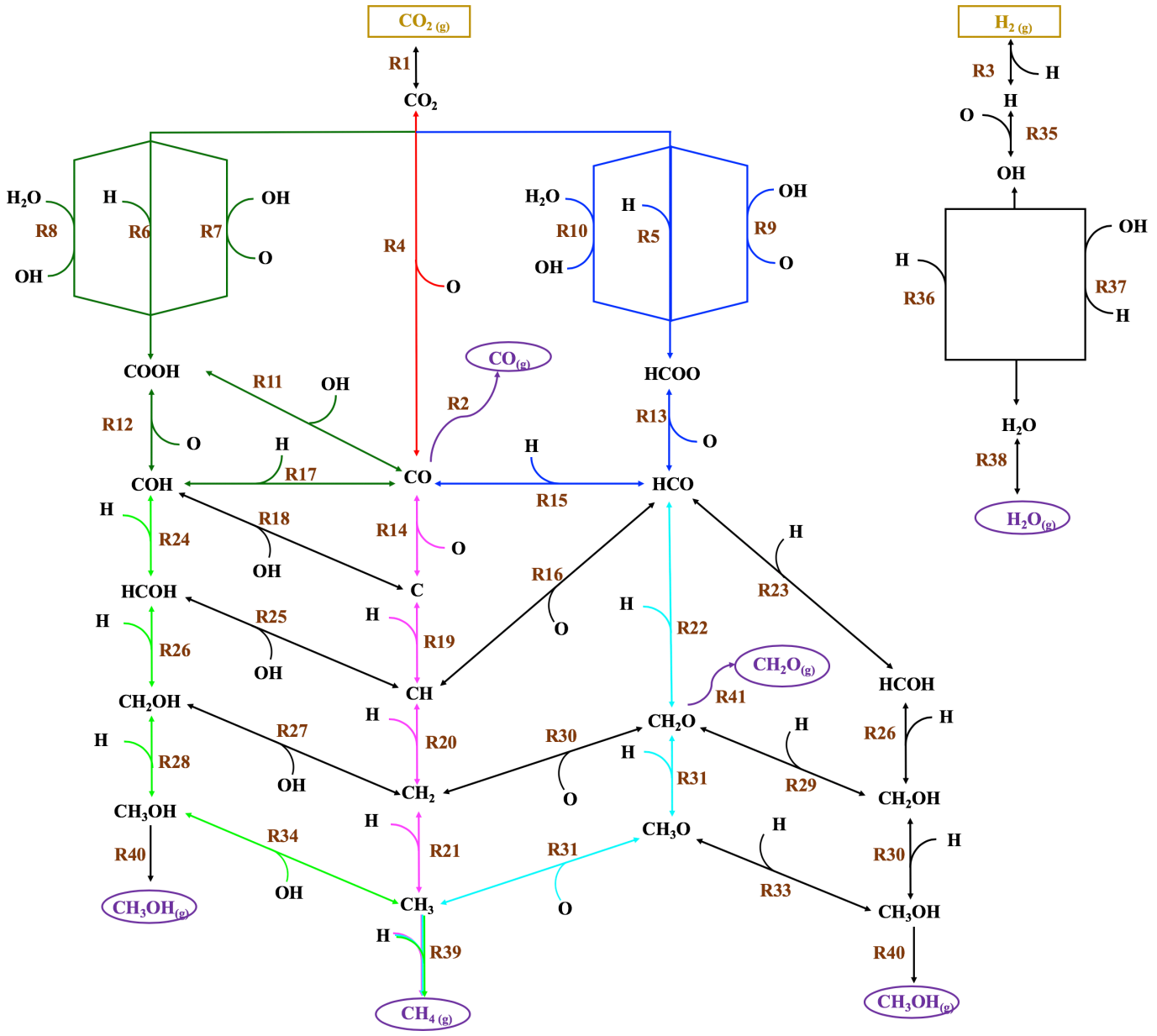

Figure 1. Reaction network proposed for the CO_2 hydrogenation (left) and H_2 oxidation (right). The redox pathway (red), formate pathway (dark blue) and carboxyl pathway (dark green) are considered for the RWGS reaction. The C hydrogenation pathway (magenta), HCO hydrogenation pathway (light blue) and COH hydrogenation pathway (light green) are considered for the Sabatier reaction. Black lines are for elementary steps that interconnect different pathways. Dark yellow and purple stands for reactants and products of the CO_2 hydrogenation reactions. Reversible steps are represented by double arrows.

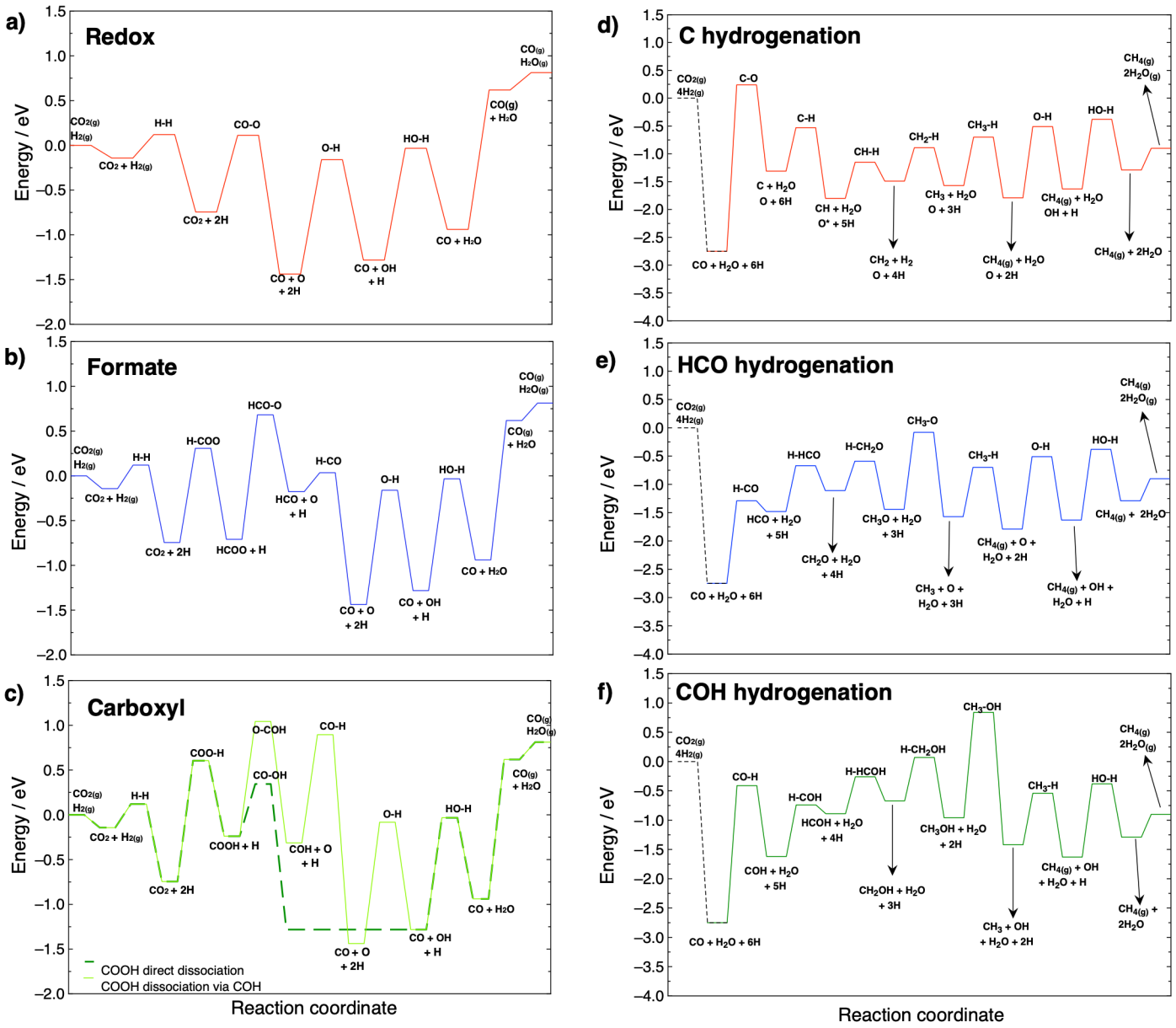

Figure 2. Potential energy diagrams corresponding to the RWGS reaction: a) redox mechanism, b) formate mechanism, c) carboxyl mechanism and the Sabatier reaction d) C hydrogenation mechanism, e) HCO hydrogenation mechanism, f) COH hydrogenation mechanism. All values include the zero-point energy term, and coadsorbed species are assumed to be at infinite distance.

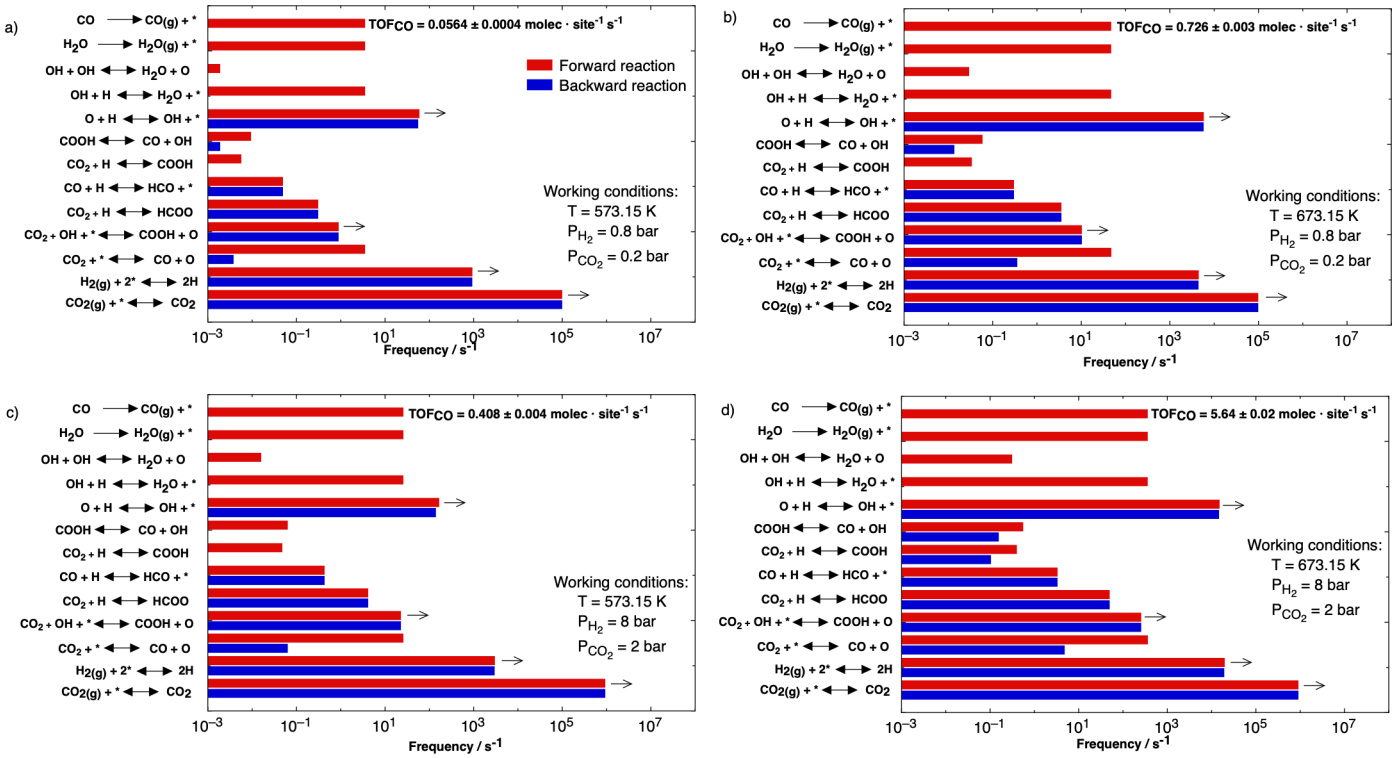

Figure 3. Event frequency of the CO_2 hydrogenation reaction at four different working conditions. a) T= 573.15 K, P_{H_2}= 0.8 bar, P_{CO_2}= 0.2 bar, b) T= 573.15 K, P_{H_2}= 8 bar, P_{CO_2}= 2 bar, c) T= 673.15 K, P_{H_2}= 0.8 bar, P_{CO_2}= 0.2 bar, d) T= 673.15 K, P_{H_2}= 8 bar, P_{CO_2}= 2 bar.

REFERENCES

(1) Barbir, F. Transition to Renewable Energy Systems with Hydrogen as an Energy Carrier. *Energy* **2009**, *34*, 308–312.

(2) Dincer, I. Renewable Energy and Sustainable Development: a Crucial Review. *Renew. Sust. Energ. Rev.* **2000**, *4,* 157–175.

(3) Jalama, K. Carbon Dioxide Hydrogenation over Nickel-, Ruthenium-, and Copper-based Catalysts: Review of Kinetics and Mechanism. *Catal. Rev.* 2017, *59*, 95–164.

(4) Kattel, S.; Liu, P.; Chen, J. G. Tuning Selectivity of CO_2 Hydrogenation Reactions at the Metal/Oxide Interface. *J. Am. Chem. Soc.* **2017**, *139*, 9739–9754.

(5) Li, W.; Wang, H.; Jiang, X.; Zhu, J.; Liu, Z.; Guo, X.; Song, C. A Short Review of Recent Advances in CO_2 Hydrogenation to Hydrocarbons over Heterogeneous Catalysts. *RSC Adv*. 2018, *8,* 7651–7669.

(6) Wang, W.; Wang, S.; Ma, X.; Gong, J. Recent Advances in Catalytic Hydrogenation of Carbon Dioxide. *Chem. Soc. Rev*. **2011**, *40*, 3703-3727.

(7) Nie, X.; Li, W.; Jiang, X.; Guo, X.; Song, C. Recent Advances in Catalytic CO_2 Hydrogenation to Alcohols and Hydrocarbons. *Adv. Catal.* **2019**, *65,* 121-133.

(8) Pirngruber, G.D.; Raybaud, P.; Belmabkhout, Y.; Čejka, J.; Zukal, A. The Role of the Extra-framework Cations in the Adsorption of CO_2 on Faujasite Y. *Phys. Chem. Chem. Phys*. **2010**, *12*, 13534-13546.

(9) Yang, H.; Xu, Z.; Fan, M.; Gupta, R.; Slimane, R.B.; Bland, A.E.; Wright, I. Progress in Carbon Dioxide Separation and Capture: A Review. *J. Environ. Sci*. **2008**, *20* 14–27.

(10) Lv, Y.X.; Yan, G.H.; Xu, C.Q.; Xu, M.; Sun, L. Review on Membrane Technologies for Carbon Dioxide Capture from Power Plant Flue Gas. *AMR.* **2012**, *602–604,* 1140–1144.

(11) Centi, G.; Quadrelli, E.A.; Perathoner, S. Catalysis for CO_2 Conversion: a Key Technology for Rapid Introduction of Renewable Energy in the Value Chain of Chemical Industries. *Energy Environ. Sci*. **2013**, *6*, 1711-1731.

(12) Götz, M.; Lefebvre, J.; Mörs, F.; Koch, A.M.; Graf, F.; Bajohr, S.; Reimert, R.; Kolb, R. Renewable Power-to-Gas: A Technological and Economic Review. *Renewable Energy.* **2016**, *85*, 1371-1390.

(13) Hartadi, Y.; Widmann, D.; Behm, R.J. CO_2 Hydrogenation to Methanol on Supported Au Catalysts under Moderate Reaction Conditions: Support and Particle Size Effects. *ChemSusChem*. **2015**, *8*, 456–465.

(14) Yang, X.; Kattel, S.; Senanayake, S.D.; Boscoboinik, J.A.; Nie, X.; Graciani, J.; Rodriguez, J.A.; Liu, P.; Stacchiola, D.J.; Chen, J.G. Low Pressure CO_2 Hydrogenation to Methanol over Gold Nanoparticles Activated on a CeO_x /TiO_2 Interface. *J. Am. Chem. Soc.* **2015**, *137*, 10104–10107.

(15) Sakurai, H.; Haruta, M. Synergism in Methanol Synthesis from Carbon Dioxide over Gold Catalysts Supported on Metal Oxides. *Catal. Today*. **1996**, *29*, 361–365.

(16) Qu, J.; Zhou, X.; Xu, F.; Gong, X.Q.; Tsang, S.C.E. Shape Effect of Pd-promoted Ga_2O_3 Nanocatalysts for Methanol Synthesis by CO_2 Hydrogenation. *J. Phys. Chem. C*. **2014**, *118*, 24452–24466.

(17) Bahruji, H.; Bowker, M.; Hutchings, G.; Dimitratos, N.; Wells, P.; Gibson, E.; Jones, W.; Brookes, C.;

Morgan, D.; Lalev, G. Pd/ZnO Catalysts for Direct CO_2 Hydrogenation to Methanol. *J. Catal.* **2016**, *343,* 133–146.

(18) Kuld, S.; Thorhauge, M.; Falsig, H.; Elkjær, C.F.; Helveg, S.; Chorkendorff, I.; Sehested, J. Quantifying the Promotion of Cu Catalysts by ZnO for Methanol Synthesis. *Science.* **2016**, *352*, 969–974.

(19) Studt, F.; Behrens, M.; Kunkes, E.L.; Thomas, N.; Zander, S.; Tarasov, A.; Schumann, J.; Frei, E.; Varley, J.B.; Abild-Pedersen, F.; Nørskov, J.K.; Schlögl, R. The Mechanism of CO and CO_2 Hydrogenation to Methanol over Cu-Based Catalysts. *ChemCatChem*. **2015**, *7*, 1105–1111.

(20) Kattel, S.; Ramírez, P.J.; Chen, J.G.; Rodriguez, J.A.; Liu, P. Active Sites for CO_2 Hydrogenation to Methanol on Cu/ZnO Catalysts. *Science.* **2017**, *355*, 1296–1299.

(21) Martin, O.; Mondelli, C.; Cervellino, A.; Ferri, D.; Curulla-Ferré, D.; Pérez-Ramírez, L. Operando Synchrotron X-ray Powder Diffraction and Modulated-excitation Infrared Spectroscopy Elucidate the CO_2 Promotion on a Commercial Methanol Synthesis Catalyst. *Angew. Chem. Int. Edit*. **2016**, *55*, 11031–11036.

(22) van den Berg, R.; Prieto, G.; Korpershoek, G.; van der Wal, L.I.; van Bunningen, A.J.; Lægsgaard-Jørgensen, S.; de Jongh, P.E.; de Jong, K.P. Structure Sensitivity of Cu and CuZn Catalysts Relevant to Industrial Methanol Synthesis. *Nat. Commun.* **2016**, *7*, 13057: 1-7.

(23) Lei, H.; Nie, R.; Wu, G.; Hou, Z. Hydrogenation of CO_2 to CH_3OH over Cu/ZnO Catalysts with Different ZnO Morphology. *Fuel.* **2015**, *154*, 161–166.

(24) Yu, K.P.; Yu, W.Y.; Kuo, M.C.; Liou, Y.C.; Chien, S.H. Pt/titania-nanotube: A Potential Catalyst for CO_2 Adsorption and Hydrogenation. *Appl. Catal. B-Environ*. **2008**, *84*, 112–118.

(25) Falbo, L.; Martinelli, M.; Visconti, C.G.; Lietti, L.; Bassano, C.; Deiana, P. Kinetics of CO_2 Methanation on a Ru-based Catalyst at Process Conditions Relevant for Power-to-Gas Applications. *App. Catal. B-Environ*. **2018**, *225*, 354–363.

(26) Jiménez, V.; Sánchez, P.; Panagiotopoulou, P.; Valverde, J.L.; Romero, A. Methanation of CO, CO_2 and Selective Methanation of CO, in Mixtures of CO and CO_2, over Ruthenium Carbon Nanofibers Catalysts. *App. Catal. A-Gen*. **2010**, *390*, 35–44.

(27) Eckle, S.; Anfang, H.G.; Behm, R.J. Reaction Intermediates and Side Products in the Methanation of CO and CO_2 over Supported Ru catalysts in H_2 -rich Reformate Gases. *J. Phys. Chem. C.* **2011**, *115*, 1361–1367.

(28) Park, J.N.; McFarland, E.W. A Highly Dispersed Pd–Mg/SiO_2 Catalyst Active for Methanation of CO_2. *J. Catal.* **2009**, *266,* 92–97.

(29) Chang, F.W.; Kuo, M.S.; Tsay, M.T.; Hsieh, M.C. Hydrogenation of CO_2 over Nickel Catalysts on Rice Husk Ash-alumina Prepared by Incipient Wetness Impregnation. *App. Catal. A-Gen.* **2003**, *247*, 309–320.

(30) Aziz, M.A.A.; Jalil, A.A.; Triwahyono, S.; Mukti, R.R.; Taufiq-Yap, Y.H.; Sazegar, M.R. Highly Active Ni-promoted Mesostructured Silica Nanoparticles for CO_2 Methanation. *App. Catal. B-Environ*. **2014**, *147,* 359–368.

(31) Tada, S.; Shimizu, T.; Kameyama, H.; Haneda, T.; Kikuchi, R. Ni/CeO_2 Catalysts with High CO_2 Methanation Activity and High CH_4 Selectivity at Low Temperatures. *Int. J. Hydrogen Energ*. **2012**, *37*, 5527–

5531.

(32) Ocampo, F.; Louis, B.; Kiwi-Minsker, L.; Roger, A.C. Effect of Ce/Zr Composition and Noble Metal Promotion on Nickel Based CexZr1−xO$_2$ Catalysts for Carbon Dioxide Methanation. *App. Catal. A-Gen.* **2011**, *392*, 36–44.

(33) Zhou, G.; Liu, H.; Cui, K.; Xie, H.; Jiao, Z.; Zhang, G.; Xiong, K.; Zheng, X. Methanation of Carbon Dioxide over Ni/CeO$_2$ catalysts: Effects of Support CeO$_2$ Structure. *Int. J. Hydrogen Energ*. **2017**, *42*, 16108–16117.

(34) Hwang, S.; Hong, U.G.; Lee, J.; Baik, J.H.; Koh, D.J.; Lim, H.; Song, I.K. Methanation of Carbon Dioxide over Mesoporous Nickel–M–alumina (M = Fe, Zr, Ni, Y, and Mg) Xerogel Catalysts: Effect of Second Metal. *Catal. Lett*. **2012**, *142*, 860–868.

(35) Heine, C.; Lechner, B.A.J; Bluhm, H.; Salmeron, M. Recycling of CO$_2$: Probing the Chemical State of The Ni(111) Surface During the Methanation Reaction with Ambient-pressure X-ray Photoelectron Spectroscopy. *J. Am. Chem. Soc*. **2016**, *138*, 13246–13252.

(36) Muroyama, H.; Tsuda, Y.; Asakoshi, T.; Masitah, H.; Okanishi, T.; Matsui, T.; Eguchi, K. Carbon Dioxide Methanation over Ni Catalysts Supported on Various Metal Oxides. *J. Catal*. **2016**, *343*, 178–126.

(37) Kattel, S.; Yan, B.; Chen, J.G.; Liu, P. CO$_2$ Hydrogenation on Pt, Pt/SiO$_2$ and Pt/TiO$_2$: Importance of Synergy between Pt and Oxide Support. *J. Catal.* **2016**, *343*, 115–126.

(38) Kusama, H.; Bando, K.K.; Okabe, K.; Arakawa, H. CO$_2$ Hydrogenation Reactivity and Structure of Rh/SiO$_2$ Catalysts Prepared from Acetate, Chloride and Nitrate Precursors. *App. Catal. A-Gen*. **2001**, *205,* 285–294.

(39) Kharaji, A.G.; Shariati, A.; Takassi, M.A. A Novel γ-alumina Supported Fe-Mo Bimetallic Catalyst for Reverse Water Gas Shift Reaction. *Chinese J. Chem. Eng*. **2013**, *21*, 1007–1014.

(40) Yang, L.; Pastor-Pérez, L.; Gu, S.; Sepúlveda-Escribano, A.; Reina, T.R. Highly Efficient Ni/CeO$_2$-Al$_2$O$_3$ Catalysts for CO$_2$ Upgrading Via Reverse Water-gas Shift: Effect of Selected Transition Metal Promoters. *App. Catal. B-Environ*. **2018**, *232*, 464–471.

(41) Sun, F.; Yan, C.; Wang, Z.; Guo, C.; Huang, S. Ni/Ce–Zr–O Catalyst for High CO$_2$ Conversion During Reverse Water Gas Shift Reaction (RWGS). *Int. J. Hydrogen Energ*. **2015**, *40*, 15985–15993.

(42) Aziz, M.A.A.; Jalil, A.A.; Triwahyono, S.; Ahmad, A. CO$_2$ Methanation over Heterogeneous Catalysts: Recent Progress and Future Prospects*. Green Chem*. **2015**, *17,* 2647–2663.

(43) Wei, W.; Jinlong, G. Methanation of Carbon Dioxide: an Overview. *Front. Chem. Sci. Eng*. **2011**, *5,* 2–10.

(44) Zhi, C.; Wang, Q.; Wang, B.; Li, D.; Zhang, R. Insight into the Mechanism of Methane Synthesis from Syngas on a Ni(111) Surface: a Theoretical Study. *RSC Adv.* **2015**, *5*, 66742–66756.

(45) Zhou, M.; Liu, B. DFT Investigation on the Competition of the Water-gas Shift Reaction ersus Methanation on Clean and Potassium-modified Nickel(111) Surfaces. *ChemCatChem.* **2015**, *7*, 3928–3935.

(46) Choe, S.J.; Kang, H.J.; Kim, S.J.; Park, S.B.; Park, D.H.; Huh, D.S. Adsorbed Carbon Formation and

Carbon Hydrogenation for CO_2 Methanation on the Ni(111) Surface: ASED-MO Study. *Bull Korean Chem. Soc*. **2005**, *26*, 1682-1688.

(47) Ren, J.; Guo, H.; Yang, J.; Qin, Z.; Lin, J.; Li, Z. Insights into the Mechanisms of CO_2 Methanation on Ni(111) Surfaces by Density Functional Theory. *Appl. Surf. Sci.* **2015**, *351*, 504–516.

(48) Vogt, C.; Monai, M.; Sterk, E.B.; Palle, J.; Melcherts, A.E.M.; Zijlstra, B.; Groeneveld, E.; Berben, P.H.; Boereboom, J.M.; Hensen, E.J.M.; Meirer, F.; Filot, I.A.W.; Weckhuysen, B.M. Understanding Carbon Dioxide Activation and Carbon‑carbon Coupling over Nickel. *Nat. Comm*. **2019**, *10*, 5330.

(49) Zhang, M.; Zijlstra, B.; Filot, I.A.W.; Li, F.; Wang, H.; Li, J.; Hensen, E.J.M. A theoretical Study of the Reverse Water-gas Shift Reaction on Ni(111) and Ni(311) Surfaces. *Can. J. Chem. Eng*. **2020**, *98*, 740-748.

(50) Dietz, L.; Piccinin, S.; Maestri, M.; Mechanistic Insights into CO_2 Activation Via Reverse Water-gas shift on Metal Surfaces. J. *Phys. Chem. C*. **2015**, *119*, 4959-4966.

(51) Blaylock, D.W.; Ogura, T.; Green, W.H.; Beran, G.J.O. Computational Investigation of Thermochemistry and Kinetics of Steam Methane Reforming on Ni(111) under Realistic Conditions. *J. Phys. Chem. C.* **2009**, *113*, 4898–4908.

(52) Catapan, R.C.; Oliveira, A.M.M.; Chen, Y.; Vlachos, D.G. DFT Study of the Water–gas shift Reaction and Coke Formation on Ni(111) and Ni(211) surfaces. *J. Phys. Chem. C.* **2012**, *116*, 20281–20291.

(53) Vrijburg, W.L.; Moioli, E.; Chen, W.; Zhang, M.; Terlingen, B.J.P.; Zijlstra, B.; Filot, I.A.W.; Züttel, A.; Pidko, E.A.; Hensen, E.J.M. Efficient Base-metal NiMn/TiO_2 Catalyst for CO_2 Methanation. *ACS. Catal*. **2019**, *9*, 7823-7839.

(54) Kresse, G.; Hafner, J. Ab Initio Molecular Dynamics for Liquid Metals. *Phys. Rev. B.* **1993**, *47*, 558–561.

(55) Kresse, G.; Furthmüller, J. Efficient Iterative Schemes for Ab Initio Total-energy Calculations Using a Plane-wave Basis Set. *Phys. Rev. B.* **1996**, *54*, 11169–11186.

(56) Kresse, G.; Furthmüller, J. Efficiency of Ab-initio Total Energy Calculations for Metals and Semiconductors Using a Plane-wave Basis Set. *Comp. Mater. Sci*. **1996**, *6*, 15–50.

(57) Kresse, G.; Joubert, D. From Ultrasoft Pseudopotentials to the Projector Augmented-wave Method. *Phys. Rev. B*. **1999**, *59,* 1758–1775.

(58) Wellendorff, J.; Silbaugh, T.L.; Garcia-Pintos, D.; Nørskov, J.K.; Bligaard, T.; Studt, F.; Campbell, C.T. A Benchmark Database for Adsorption Bond Energies to Transition Metal Surfaces and Comparison to Selected DFT Functionals. *Surf. Sci*. **2015**, *640*, 36-44.

(59) Campbell, C.T. Energies of Adsorbed Catalytic Intermediates on Transition Metal Surfaces: Calorimetric Measurements and Benchmarks for Theory. *Acc. Chem. Res*. **2019**, *52*, 984–993.

(60) Gautier, S.; Steinmann, S.N.; Michel, C.; Fleurat-Lessard, P.; Sautet, P. Molecular Adsorption at Pt(111). How Accurate are DFT functionals?. *Phys. Chem. Chem. Phys*. **2015**, *17*, 28921-28930.

(61) Wellendorff, J.; Lundgaard, K.T.; Møgelhøj, A.; Petzold, V.; Landis, D.D.; Nørskov, J.K.; Bligaard, T.; Jacobsen, K.W. Density Functionals for Surface Science: Exchange-correlation Model Development with Bayesian Error Estimation. *Phys. Rev. B.* **2012**, *85*, 235149:1-23.

(62) Kittle, C. Introduction to Solid State Physics, Wiley, NY, 6th edn, **1986**.

(63) Monkhorst, H.J.; Pack, J.D. Special Points for Brillouin-zone Integrations. *Phys. Rev. B*. **1976**, *13*, 5188–5192.

(64) Jónsson, H.; Mills, G.; Jacobsen, K.W. Nudged Elastic Band Method for Finding Minimum Energy Paths of Transitions, in: Classical and Quantum Dynamics in Condensed Phase Simulations, World scientific, Lerici, Villa Marigola, **1998**, 385–404.

(65) Henkelman, G.; Uberuaga, B.P.; Jónsson, H. A Climbing Image Nudged Elastic Band Method for Finding Saddle Points and Minimum Energy Paths, *J. Chem. Phys.* **2000**, *113*, 9901–9904.

(66) Hjorth Larsen, A.; Jørgen Mortensen, J.; Blomqvist, J.; Castelli, I.E.; Christensen, R.; Dułak, M.; Friis, J.; Groves, M.N.; Hammer, B.; Hargus, C.; Hermes, E.D.; Jennings, P.C.; Bjerre Jensen, P.; Kermode, J.; Kitchin, J.R.; Leonhard Kolsbjerg, E.; Kubal, J.; Kaasbjerg, K.; Lysgaard, S.; Bergmann Maronsson, J.; Maxson, T.; Olsen, R.; Pastewka, L.; Peterson, A.; Rostgaard, C.; Schiøtz, J.; Schütt, O.; Strange, M.; Thygesen, K.S.; Vegge, T.; Vilhelmsen, L.; Walter, M.; Zeng, Z.; Jacobsen, K.W. The Atomic Simulation Environment—a Python Library for Working with Atoms. *J. Phys.: Condens. Matter*. **2017**, *29,* 273002.

(67) Smidstrup, S.; Pedersen, A.; Stokbro, K.; Jónsson, H. Improved Initial guess for Minimum Energy Path Calculations. *J. Chem. Phys.* **2014**, *140*, 214106:1-6.

(68) Andersen, M.; Panosetti, C.; Reuter, K.; A Practical Guide to Surface Kinetic Monte Carlo Simulations. *Front. Chem*. **2019**, *7*, 202:1-24.

(69) Prats, H.; Illas, F.; Sayós, R. General Concepts, Assumptions, Drawbacks and Misuses in Kinetic Monte Carlo and Microkinetic Modelling Simulations Applied to Computational Heterogeneous Catalysis. *Int. J. Quant. Chem*. **2018**, *118,* e25518:1-14

(70) Stamatakis, M.; Vlachos, D.G.; A Graph-theoretical Kinetic Monte Carlo Framework for on-lattice Chemical Kinetics. *J. Chem. Phys*. **2011**, *134*, 214115:1-13.

(71) Stamatakis, M.; Vlachos, D.G.; Unraveling the Complexity of Catalytic Reactions Via kinetic Monte Carlo Simulation: Current Status and Frontiers. *ACS Catal*. **2012**, *2*, 2648–2663.

(72) Nielsen, J.; d'Avezac, M.; Hetherington, J.; Stamatakis, M.; Parallel kinetic Monte Carlo Simulation Framework Incorporating Accurate Models of Adsorbate Lateral Interactions. *J. Chem. Phys*. **2013**, *139*, 224706:1-13.

(73) Yang, L.; Karim, A.; Muckerman, J.T. Density Functional Kinetic Monte Carlo Simulation of Water–gas Shift Reaction on Cu/ZnO. *J. Phys. Chem. C*. **2013**, *117*, 3414–3425.

(74) Prats, H.; Álvarez, L.; Illas, F.; Sayós, R. Kinetic Monte Carlo Simulations of the Water Gas Shift reaction on Cu(1 1 1) From Density Functional Theory Based Calculations. *J. Catal.* **2016**, *333,* 217–226.

(75) Piccinin, S.; Stamatakis, M. CO Oxidation on Pd(111): a First-principles-based Kinetic Monte Carlo Study. *ACS Catal.* **2014**, *4,* 2143–2152.

(76) Prats, H.; Posada-Pérez, S.; Rodriguez, J.A.; Sayós, R.; Illas, F. Kinetic Monte Carlo Simulations Unveil Synergic Effects at Work on Bifunctional Catalysts. *ACS Catal*. **2019**, *9*, 9117–9126.

(77) Stuckless, J.T.; AlSarraf, N.; Wartnaby, C.; King, D.A. Calorimetric Heats of Adsorption for CO on Nickel Single Crystal Surfaces. *J. Chem. Phys*. **1993**, *99,* 2202-2212.

(78) Beniya, A.; Isomura, N.; Hirata, H.; Watanabe, Y. Low Temperature Adsorption and Site-conversion Process of CO on the Ni(111) Surface. *Surf. Sci*. **2012**, *606*, 1830-1836.

(79) Prats, H.; Gamallo, P.; Sayós, R.; Illas, F. Unexpectedly Large Impact of Van der Waals Interactions on the Description of Heterogeneously Catalyzed Reactions: the Water Gas Shift Reaction on Cu(321) as a Case Example. *Phys. Chem. Chem. Phys*. **2016**, *18*, 2792–2801.

(80) Campbell, C.T. The Degree of Rate Control: a Powerful Tool for Catalysis Research. *ACS Cata*l. **2017**, *7*, 2770–2779.